PROCEEDINGS OF SPIE

SPIEDigitalLibrary.org/conference-proceedings-of-spie

Computational integration of renal histology and urinary proteomics using neural networks

Nicholas Lucarelli, Donghwan Yun, Dohyun Han, Brandon Ginley, Kyung Chul Moon, et al.

Nicholas Lucarelli, Donghwan Yun, Dohyun Han, Brandon Ginley, Kyung Chul Moon, Avi Rosenberg, John Tomaszewski, Seung Seok Han, Pinaki Sarder, "Computational integration of renal histology and urinary proteomics using neural networks," Proc. SPIE 12039, Medical Imaging 2022: Digital and Computational Pathology, 120390U (4 April 2022); doi: 10.1117/12.2613500

SPIE.

Event: SPIE Medical Imaging, 2022, San Diego, California, United States

Computational Integration of Renal Histology and Urinary Proteomics using Neural Networks

Nicholas Lucarelli[a]*, Donghwan Yun[b*], Dohyun Han[c*], Brandon Ginley[a], Kyung Chul Moon[b], Avi Rosenberg[d], John Tomaszewski[a], Seung Seok Han[b,+], and Pinaki Sarder[a,+]

[a]Department of Pathology and Anatomical Sciences, University at Buffalo – The State University of New York, Buffalo, New York; [b]Department of Internal Medicine, Seoul National University College of Medicine, Seoul, Korea; [c]Proteomics Core Facility, Biomedical Research Institute, Seoul National University Hospital, Seoul, Korea; [d]Department of Pathology, Johns Hopkins University School of Medicine, Baltimore, Maryland

* indicates equal contributions
+ Corresponding authors:
Seung Seok Han, MD, PhD (Email: hansway7@snu.ac.kr)
Pinaki Sarder, PhD (Email: pinakisa@buffalo.edu)

ABSTRACT

Histological image data and molecular profiles provide context into renal condition. Often, a biopsy is drawn to diagnose or monitor a suspected kidney problem. However, molecular profiles can go beyond a pathologist's ability to see and diagnose. Using AI, we computationally incorporated urinary proteomic profiles with microstructural morphology from renal biopsy to investigate new and existing molecular links to image phenotypes.

We studied whole slide images of periodic acid-Schiff stained renal biopsies from 56 DN patients matched with 2,038 proteins measured from each patient's urine. Using Seurat, we identified differentially expressed proteins in patients that developed end-stage renal disease within 2 years of biopsy. Glomeruli, globally sclerotic glomeruli, and tubules were segmented from WSI using our previously published HAIL pipeline. For each glomerulus, 315 handcrafted digital image features were measured, and for tubules, 207 features. We trained fully connected networks to predict urinary protein measurements that were differentially expressed between patients who did/ did not progress to ESRD within 2 years of biopsy. The input to this network was either glomerular or tubular histomorphological features in biopsy. Trained network weights were used as a proxy to rank which morphological features correlated most highly with specific urinary proteins.

We identified significant image feature-protein pairs by ranking network weights by magnitude. We also looked at which features on average were most significant in predicting proteins. For both glomeruli and tubules, RGB color values and variance in PAS^+ areas (specifically basement membrane for tubules) were, on average, more predictive of molecular profiles than other features.

There is a strong connection between molecular profile and image phenotype, which can be elucidated through computational methods. These discovered links can provide insight to disease pathways, and discover new factors contributing to incidence and progression.

Keywords: Artificial Intelligence (AI), Diabetic Nephropathy (DN), Urinary Proteomics, Digital Pathology.

1. INTRODUCTION

Type II diabetic nephropathy (DN) is one of the leading drivers of chronic kidney disease and end-stage renal disease worldwide [1]. The incidence of type II DN is increasing due to a high prevalence of diabetes, where complications such

Medical Imaging 2022: Digital and Computational Pathology, edited by John E. Tomaszewski,
Aaron D. Ward, Proc. of SPIE Vol. 12039, 120390U · © 2022 SPIE
1605-7422 · doi: 10.1117/12.2613500

as proteinuria, and decline in kidney function affect more than 40% of patients [2-4]. The heterogenous nature of type II DN further complicates a comprehensive approach to treating patients, and many patients often require dialysis within a few years of diabetes diagnosis [5]. In many cases, patients are diagnosed with CKD too late, where progression to ESRD is highly likely, and is associated with higher mortality and morbidity[6].

Renal biopsy is the current gold standard for the diagnosis and monitoring of kidney disease, but has its drawbacks in terms of subjectivity and reproducibility. Due to variance in place of education, and levels of talent and experience, various pathologists can have differing opinions on what is seen in a biopsy. This issue is commonly mediated by obtaining multiple opinions, but this is not always possible in renal histopathology. Therefore, the possibility of diagnostic error is introduced, which may lead to incorrect treatment and worse clinical outcomes.

Molecular profiles have the ability to go beyond a pathologist's ability to see and diagnose. Urinary proteomics are commonly used in biomarker discovery in various human diseases [7], which can be used for early detection or progression monitoring [8]. They also offer a more holistic view of renal function as compared to biopsy inspection, are non-invasive, and more reproducible. As mentioned earlier, the currently understood phenotype of type II DN is heterogenous, making it difficult to determine which patients are likely to experience a rapid decline in kidney function [5].

The integration of both histopathology data and urinary proteomics is largely unexplored, but has the potential to improve our understanding of the mechanisms behind type II DN development and progression, leading to more informed clinical decisions. Moreover, it is a critical link to translate molecular findings into real clinical applicability. Recently, the use of computational methods of analysis and artificial intelligence (AI) in medical imaging have increased [9], demonstrating potential to augment clinical precision and improve efficiency. Some applications of AI in medical imaging involve the use of convolutional neural network (CNN)-derived image features for analyses [10]. While these have shown promise in some applications, they are limited because the reasons behind their decisions are not clearly interpretable. However, we have shown that bioengineered image histomorphometric features have significant value in quantifying renal biopsies[11, 12]. Using artificial intelligence, we can computationally correlate urinary proteins with morphological changes in renal biopsies, to investigate new and existing molecular links to image phenotypes.

2. METHODS

2.1 Patient and Image Data

Type II DN patients were sourced from Seoul National University Hospital. Some patient demographic and medical history information was provided, including age, sex, height, weight, history of diabetes, and presence of diabetic retinopathy and hypertension.

Images consisted of whole-slide images (WSIs) of Periodic Acid-Schiff (PAS)-stained renal biopsies from type II DN patients ($n = 56$).

2.2 Urinary Proteomics

For protein digestion, 1-2 ml of each urine sample was concentrated to 250 ul using a spin filter with a molecular weight cut-off of 3 kDa (Millipore, Billerica, MA, USA). The protein concentration was measured according to the Bradford assay protocol (BioRad protein assay kit, BioRad). For protein digestion, 50 ug of urine proteins were precipitated by adding a 5-fold volume of ice-cold acetone. The precipitated samples were reconstituted in 50 ul of SDT buffer (2% SDS, 0.1M dithiothreitol in 0.1M Tris HCl; pH, 8.0). After being heated at 95°C, the denatured proteins were digested by a filter-aided sample preparation method as the previously described [13] with some modifications. Briefly, protein samples were loaded onto a 30K amicon filter (Millipore, Billerica, MA, USA), and buffer was exchanged with UA solution (8 M urea in 0.1M Tris-HCl; pH, 8.5) via centrifugation. After three buffer exchange with UA solution, the reduced cysteines were alkylated with 0.05 M iodoacetamide in UA solution for 30 min at room temperature in the dark. Thereafter, UA buffer was exchanged for 40 mM ammonium bicarbonate (ABC) twice. The protein samples were digested with trypsin/Lys-C (enzyme to substrate ratio of 1:100) at 37°C for 16 h. The resulting peptides were collected to new tube via centrifugation, and an additional elution step was performed using 40 mM ABC and 0.5 M NaCl. All resulting peptides were acidified with 10% trifluoroacetic acid and desalted using a homemade styrenedivinylbenzene reversed-phase sulfonate (SDB-RPS)-StageTips as described [14, 15]. The peptides were initially washed with 0.2% TFA, and were then sequentially eluted with 40%, 60%, and 80% acetonitrile containing 1% ammonia. Fractionated peptides were completely dried with a vacuum dryer and stored at -80°C.

To construct a matching spectral library for matching between runs, pooled urine samples were digested using the 2-step filter-aided sample preparation as described previously [15, 16]. Digested peptides were desalted using Oasis HLB solid-phase extraction. For the in-depth data set, 100 µg of purified peptides were fractionated using an Agilent 1260 Bio-Inert HPLC (Agilent Technologies) equipped with an analytical column (4.6 × 250 mm, 5-µm particle). High-pH reversed-phase peptide fractionation was performed at a flow rate of 0.8 ml/min over a 60-min gradient using solvent A (15 mm ammonium hydroxide in water) and solvent B (15 mM ammonium hydroxide in 90% acetonitrile). A total of 96 fractions was collected each minute and non-contiguously pooled into 24 fractions. The fractions were dried in a vacuum centrifuge and stored at -80°C until liquid chromatography-tandem mass spectrometry (LC-MS/MS) analysis.

LC-MS/MS analysis methods were performed using Quadrupole Orbitrap mass spectrometers, Q-exactive plus (Thermo Fisher Scientific, Waltham, MA, USA) coupled to an Ultimate 3000 RSLC systems (Dionex, Sunnyvale, CA, USA) with a nano electrospray source as previously described with some modifications [13, 14]. Peptide samples were separated on the 2-column setup with a trap column (300 µm I.D. × 0.5 cm, C18 3 µm, 100 Å) and analytical column (50 µm I.D. × 50 cm, C18 1.9 µm, 100 Å). Prior to sample injection, the dried peptide samples were redissolved in solvent A (2% acetonitrile and 0.1% formic acid). After the samples were loaded onto the nano LC, a 90-min gradient from 8% to 30% solvent B (100% acetonitrile and 0.1% formic acid) was applied to all samples. The spray voltage was 2.0 kV in positive ion mode and the temperature of the heated capillary was set to 320°C. Mass spectra were acquired in data-dependent mode using a top 15 method on a Q Exactive. The Orbitrap analyser scanned precursor ions with a mass range of 300–1650 m/z and resolution of 70,000 at m/z 200. Higher-energy collisional dissociation scans were acquired on the Q Exactive at a resolution of 17,500. HCD peptide fragments were acquired at a normalized collision energy of 28. The maximum ion injection times for the survey and MS/MS scans were 20 and 120 ms, respectively.

Mass spectra were processed with MaxQuant (version 1.6.1.0) [17]. MS/MS spectra were searched against the Human Uniprot protein sequence database (December 2014, 88,657 entries) using the Andromeda search engine [18]. Primary searches were performed using a 6-ppm precursor ion tolerance for total protein level analysis. The MS/MS ion tolerance was set to 20 ppm. Cysteine carbamidomethylation was set as a fixed modification. N-acetylation of proteins and oxidation of methionine were set as variable modifications. Enzyme specificity was set to full tryptic digestion. Peptides with a minimum length of six amino acids and up to two missed cleavages were considered. The required false discovery rate was set to 1% at the peptide, protein, and modification levels. To maximize the number of quantification events across samples, matching between runs was performed using the pooled urine sample as a library.

2.3 Whole Slide Image Segmentation

Panoptic segmentation [19] was performed on PAS-stained WSIs to classify pixels into 6 categories, and to resolve instances of the same class. These 6 categories include image background, renal interstitium, non-globally-sclerotic glomeruli, globally-sclerotic glomeruli, renal tubules, and arteries/arterioles. Medullary regions were manually annotated and excluded from analysis. Additionally, artifacted glomeruli and tubules were removed from further analyses. The panoptic network was trained on previously annotated WSIs, using our previously published, publicly available H-AI-L pipeline [20].

Using the WSI panoptic classifications, glomerular and tubular pixels were further classified into three components based on their appearance in the PAS stained biopsies: (1) nuclear components, (2) PAS^+ components, and (3) luminal components. Individual nuclei were segmented using another separately trained panoptic classifier. The PAS^+ components were then segmented by thresholding the saturation channel of the images, and the remaining unclassified pixels were classified as luminal components. Additionally, for tubules, the tubular basement membrane was segmented from the PAS+ pixels near the tubular border, and other PAS+ pixels were classified as intra-tubular objects (ITO).

For both individual glomeruli and tubules, several digital image feature types were defined, including color, texture, morphology, containment, and inter/intrastructural distances. A total of 315 image features were measured for each glomerulus, while 207 features were measured for each segmented tubule.

2.4 Fully Connected Neural Network

Using end-stage renal disease (ESRD) progression within 2 years post-biopsy as primary outcome, we identified 45 differentially measured urine proteins, using a Wilcoxon rank sum test, built-in to the state-of-the-art analysis software Seurat [21, 22]. This was done to narrow the wide scope of available proteins to those deemed relevant to the progression of DN.

Next, the measured image features were integrated using AI to predict the narrowed urinary protein measurements. Rather than measuring the network performance on a holdout set, we were interested in extracting the weights learned by the network, to investigate which image features the network deemed most important to predicting each associated urinary protein.

To predict this urinary protein output, we designed a simple fully-connected neural network (FCNN) with only one hidden layer with nodes equal to number of digital image features. For each iteration of this network architecture, a few different sets of features were used as input: (1) digital image features from non-globally-sclerotic glomeruli, (2) digital image features from globally-sclerotic glomeruli, and (3) digital image features from tubules. Each instance of glomerulus or tubule was paired with its patient level protein measurements as its label. Mean absolute error was used as the loss function for network training. The entire dataset was used to train the network, since we were interested in the learned network parameters, rather than the regression accuracy on a holdout set. Variance stabilizing normalization (VSN) [23], followed by standardization was applied to the proteomic labels. We experimented with both normal standardizations, and VSN plus standardization for the digital image features as input. Gaussian noise with $\sigma = 0.1$ was injected to both labels and features in each training step, to ease the training of the network. The network was trained until enough steps had been completed to reach convergence.

Training losses, network predictions, and the network weights were exported into CSV format, and analyzed using MATLAB. Network prediction error was calculated, and network weights were sorted by magnitude. Additionally, output prediction error was calculated against standardized proteomic labels, using mean absolute error. Lastly, spearman's rank correlation coefficients were measured between average patient predictions and proteomic label, to assess model fit.

3. RESULTS

3.1 Panoptic Segmentation

PAS-stained renal biopsies were segmented into 6 classes: background, glomeruli, globally-sclerotic glomeruli, tubules, arteries and arterioles, and interstitium. An example segmentation is shown in ***Fig. 1***.

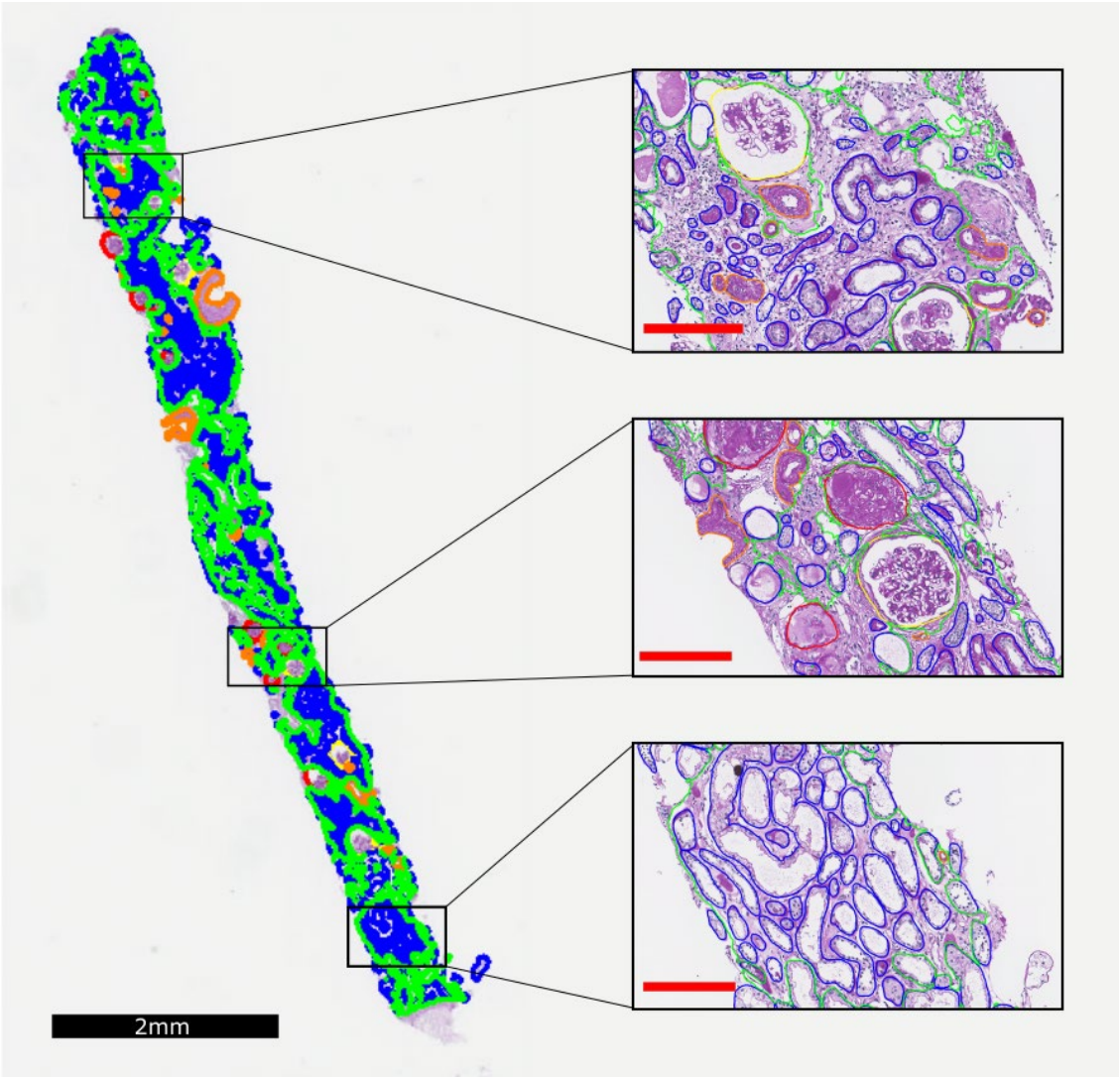

Fig. 1. Multicompartment Segmentation of Renal Biopsy. Segmentation of PAS-stained renal tissue into 6 compartments: Background (none), interstitium (green), glomeruli (yellow), globally sclerotic glomeruli (red), tubules (blue), arteries and arterioles (orange). Black scale bar: 2 mm. Red scale bars: 200 µm.

3.2 Fully Connected Neural Network

Once each of the FCNNs was fully trained, we extracted the network weights for the single hidden layer between input and output. The network contains one weight value for each digital image feature and protein pair, and these were aggregated to a grid with image features on the y-axis and proteins on the x-axis. Examples of these weight matrices can be seen in ***Fig. 2.*** From this grid, we ranked each weight according to the magnitude. Additionally, we averaged the magnitude of weights across features, and ranked each feature accordingly. This was repeated for the various neural network input feature types, which included digital image features from non-globally-sclerotic glomeruli, globally-sclerotic glomeruli, and renal tubules. Under the assumption that our normalization is robust, we should be able to compare weight coefficients, since the feature distributions will be similar. Urinary proteins in this case were used as the independent variable, and their aggregated coefficients were not considered.

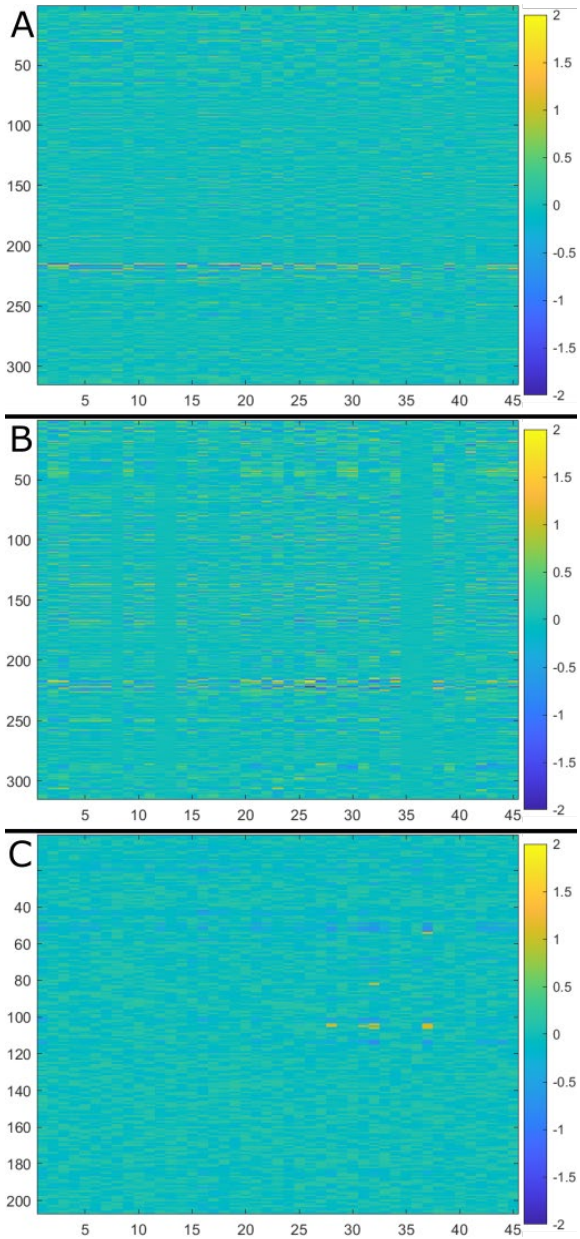

Fig. 2. Weight matrices for three fully trained Fully Connected Neural Networks (FCNN). (A) Non-globally sclerotic glomeruli, (B) globally sclerotic glomeruli, (C) Tubules. Y-axis denotes digital image features, X-axis denotes urinary proteins.

3.3 Non-Globally Sclerotic Glomeruli

The first digital image feature set analyzed was for non-globally-sclerotic glomeruli. These were identified by the panoptic network as a separate class from globally-sclerotic glomeruli. From the network predictions, the average error was 0.34, with the units as standard deviations, since these were normalized labels. The average spearman's correlation coefficient between predictions and label was 0.87, with a standard deviation of 0.10.

Across all WSIs in this cohort, 936 total glomeruli were segmented. Of these, 464 were classified as non-globally sclerotic. 315 digital image features were measured for each glomerulus, which included color features, textures, morphologies, containment, and intra/interstructural distances. Of these features, pixel color values and variances within the PAS^+ regions of the glomeruli were most significant in predicting urinary protein values. For example, on average,

the feature with the highest weighting was the "standard deviation of green values in PAS$^+$ regions". This means that the variation in green values with the PAS$^+$ sub-compartment of glomeruli was often more predictive of molecular profile than other features. This feature value can be visualized in ***Fig. 3***. The green pixel channel in an image has a strong contribution towards its perceived brightness [24], and the standard deviation is related to image contrast [25]. Image contrast reflects the different contents of an image, and in this case, the contents of the PAS$^+$ regions. Since the PAS$^+$ sub-compartment segmentation primarily captures the glomerular basement membrane, mesangium, and Bowman's capsule, this feature perhaps gives us insight to the volume filled by these compartments, and the density of molecular components. Additionally, one of the top correlated urinary proteins with this feature was C7, a protein expressed by mesangial cells [26]. Other significant features for predicting molecular profile included the variable thickness of PAS$^+$ regions.

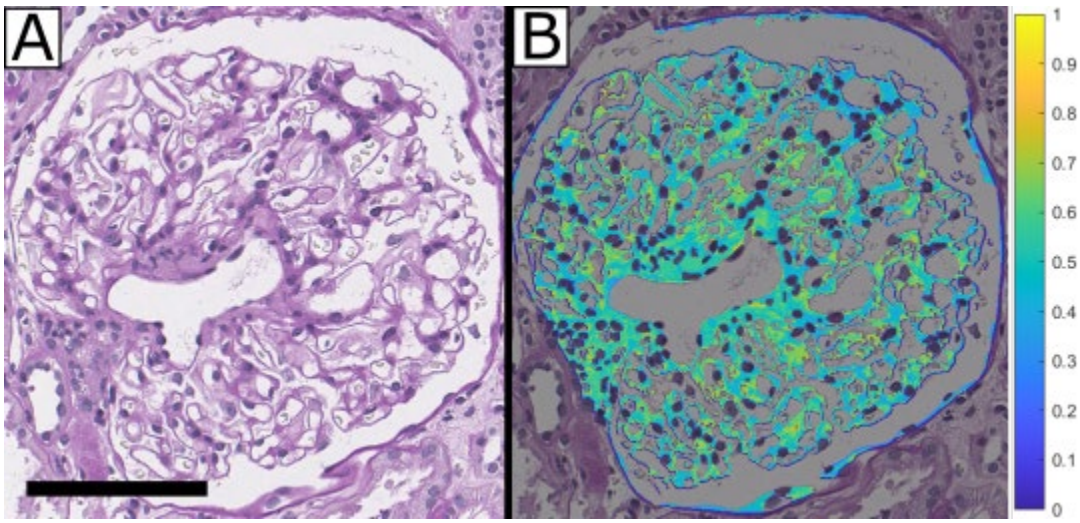

Fig. 3. Green Values in the PAS$^+$ Region. (A) The glomerulus is segmented from the rest of the biopsy. (B) Green Pixel values of the PAS$^+$ regions are shown in a heatmap with accompanied scale. Black scale bar: 100 µm.

3.4 Globally Sclerotic Glomeruli

The next image feature set analyzed was for globally-sclerotic glomeruli. This was separated from non-globally-sclerotic glomeruli to divide the analysis between earlier and late-stage kidney disease. From the network predictions, the average error was 0.44, with the units as standard deviations, since these were normalized labels. The average spearman's correlation coefficient between predictions and label was 0.81, with a standard deviation of 0.08.

Across all WSIs in this cohort, 472 of the 936 total glomeruli were globally sclerotic. The same set of 315 features were measured for these glomeruli, and ranked in the same manner. In this case, some of the most significant image features for predicting molecular profile came from the nuclei. More specifically, the mean pixel color values for each channel coming from segmented nuclear regions. Globally-sclerotic glomeruli often contain a lower density of nuclei, due to the accumulation of scar tissue. Our results suggest that as disease develops, these nuclei become darker, specifically in the blue channel. This could be due to differences in the chromatin distribution, which would cause the nuclei to stain differently. Additionally, differences in nuclei across cell types may give us insight to the distribution of these types, including glomerular specific cells, and other associated cells such as lymphocytes.

3.5 Tubules

Lastly, we also looked at an image feature set for renal tubules. From the network predictions, the average error was 0.56, with the units as standard deviations, since these were normalized labels. The average spearman's correlation coefficient between predictions and label was 0.78, with a standard deviation of 0.12.

Across all WSIs in this cohort, over 60,000 tubules were segmented, and 207 digital features were measured on each image. Similar to the glomeruli, tubular feature-protein pairs, as well as aggregate feature scores were ranked based on magnitude of their network weights. In addition to the features measured on the PAS$^+$, luminal, and nuclear regions, a

separate set of features were also measured specifically for the tubular basement membrane (TBM). An example of this segmentation is shown in ***Fig. 4***. This proved to be useful, in that most of the significant image features for predicting molecular profile came from the TBM. More specifically, the top two features by network weight magnitude were the mean green and blue pixel values in the TBM. The tubular basement membrane has often been previously implicated in disease progression [27], which supports our result that TBM morphology is indicative of molecular profile. Additionally, one of the most highly correlated proteins with these feature types is epithelial growth factor, which is expressed by tubular epithelial cells [28].

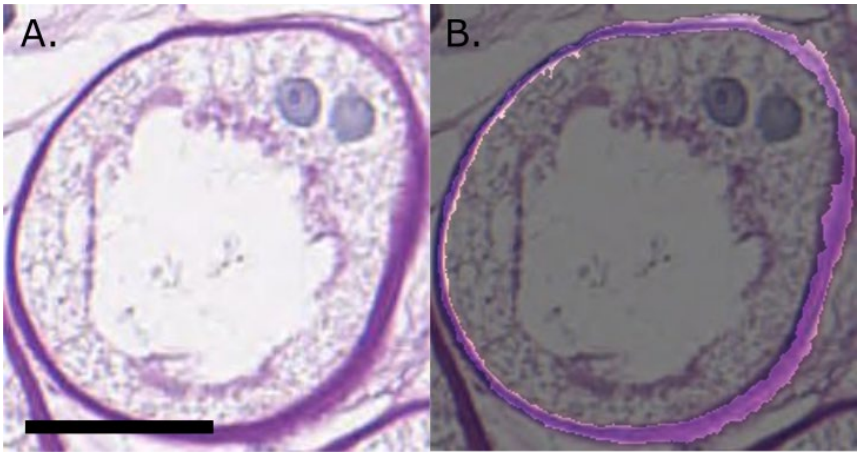

Fig. 4. Tubular Basement Membrane Segmentation. (A) The tubule is segmented from the rest of the biopsy. (B) The tubular basement membrane is segmented from the rest of the tubule, by first segmenting the PAS^+ region. Scale Bar: 25 µm.

4. CONCLUSIONS

We have demonstrated that there is a significant connection between urinary proteins and image phenotype, which we have elucidated through computational methods. This procedure is an open-ended, investigative tool that is not limited to a specific organ or stain. This could also be expanded to new feature sets for other regions/structures of interest, and could be expanded to deeper protein sets agnostic of labels, or new protein sets aligned with new labels. These discovered links can provide insight to disease pathways, and discover new factors contributing to disease incidence and progression, especially for complex disease phenotypes like type 2 DN. This can lead to more informed and consistent diagnoses and monitoring, for improved patient outcomes.

REFERENCES

1. Koye, D.N., et al., *The Global Epidemiology of Diabetes and Kidney Disease.* Adv Chronic Kidney Dis, 2018. **25**(2): p. 121-132.
2. Doshi, S.M. and A.N. Friedman, *Diagnosis and Management of Type 2 Diabetic Kidney Disease.* Clin J Am Soc Nephrol, 2017. **12**(8): p. 1366-1373.
3. Adler, A.I., et al., *Development and progression of nephropathy in type 2 diabetes: the United Kingdom Prospective Diabetes Study (UKPDS 64).* Kidney Int, 2003. **63**(1): p. 225-32.
4. Fiorentino, M., et al., *Renal biopsy in patients with diabetes: a pooled meta-analysis of 48 studies.* Nephrol Dial Transplant, 2017. **32**(1): p. 97-110.
5. Jiang, G., et al., *Progression of diabetic kidney disease and trajectory of kidney function decline in Chinese patients with Type 2 diabetes.* Kidney Int, 2019. **95**(1): p. 178-187.
6. Sprangers, B., P. Evenepoel, and Y. Vanrenterghem, *Late Referral of Patients With Chronic Kidney Disease: No Time to Waste.* Mayo Clinic Proceedings, 2006. **81**(11): p. 1487-1494.
7. Doykov, I.D., et al., *Rapid, proteomic urine assay for monitoring progressive organ disease in Fabry disease.* (1468-6244 (Electronic)).

8. Zhang, H., et al., *Identification of urine protein biomarkers with the potential for early detection of lung cancer.* Scientific Reports, 2015. **5**(1): p. 11805.
9. Pesapane, F., M. Codari, and F. Sardanelli, *Artificial intelligence in medical imaging: threat or opportunity? Radiologists again at the forefront of innovation in medicine.* European Radiology Experimental, 2018. **2**(1): p. 35.
10. Fu, Y., et al., *Pan-cancer computational histopathology reveals mutations, tumor composition and prognosis.* Nature Cancer, 2020. **1**(8): p. 800-810.
11. Ginley, B., et al., *Computational Segmentation and Classification of Diabetic Glomerulosclerosis.* J Am Soc Nephrol, 2019. **30**(10): p. 1953-1967.
12. Brandon, G., et al. *Fully automated classification of glomerular lesions in lupus nephritis*. in *Proc.SPIE*. 2020.
13. Grzegorski, S.J., et al., *Disruption of the kringle 1 domain of prothrombin leads to late onset mortality in zebrafish.* Scientific reports, 2020. **10**(1): p. 4049-4049.
14. Rhee, S.J., et al., *Comparison of serum protein profiles between major depressive disorder and bipolar disorder.* BMC psychiatry, 2020. **20**(1): p. 145-145.
15. Han, D., et al., *Proteomic analysis of mouse astrocytes and their secretome by a combination of FASP and StageTip-based, high pH, reversed-phase fractionation.* PROTEOMICS, 2014. **14**(13-14): p. 1604-1609.
16. Han, D., et al., *Integrated approach using multistep enzyme digestion, TiO2 enrichment, and database search for in-depth phosphoproteomic profiling.* PROTEOMICS, 2015. **15**(2-3): p. 618-623.
17. Tyanova, S., T. Temu, and J. Cox, *The MaxQuant computational platform for mass spectrometry-based shotgun proteomics.* Nature Protocols, 2016. **11**(12): p. 2301-2319.
18. Cox, J., et al., *Andromeda: A Peptide Search Engine Integrated into the MaxQuant Environment.* Journal of Proteome Research, 2011. **10**(4): p. 1794-1805.
19. Kirillov, A., et al., *Panoptic Segmentation.* 2019 IEEE/CVF Conference on Computer Vision and Pattern Recognition (CVPR), 2019: p. 9396-9405.
20. Lutnick, B., et al., *An integrated iterative annotation technique for easing neural network training in medical image analysis.* Nature Machine Intelligence, 2019. **1**(2): p. 112-119.
21. Stuart, T., et al., *Comprehensive Integration of Single-Cell Data.* Cell, 2019. **177**(7): p. 1888-1902.e21.
22. Butler, A., et al., *Integrating single-cell transcriptomic data across different conditions, technologies, and species.* Nature Biotechnology, 2018. **36**(5): p. 411-420.
23. Välikangas, T., T. Suomi, and L.L. Elo, *A systematic evaluation of normalization methods in quantitative label-free proteomics.* Briefings in bioinformatics, 2018. **19**(1): p. 1-11.
24. Bezryadin, S., P. Bourov, and D. Ilinih, *Brightness Calculation in Digital Image Processing.* International Symposium on Technologies for Digital Photo Fulfillment, 2007. **2007**: p. 10-15.
25. Moulden, B., F. Kingdom, and L. Gatley, *The Standard Deviation of Luminance as a Metric for Contrast in Random-Dot Images.* Perception, 1990. **19**: p. 79-101.
26. Guo, H., et al., *Complement C7 is Specifically Expressed in Mesangial Cells and is a Potential Diagnostic Biomarker for Diabetic Nephropathy and is Regulated by miR-494-3p and miR-574-5p.* Diabetes, Metabolic Syndrome and Obesity: Targets and Therapy, 2021. **Volume 14**: p. 3077-3088.
27. Tyagi, I., et al., *Thickness of glomerular and tubular basement membranes in preclinical and clinical stages of diabetic nephropathy.* Indian journal of nephrology, 2008. **18**(2): p. 64-69.
28. Zepeda-Orozco, D., et al., *EGF regulation of proximal tubule cell proliferation and VEGF-A secretion.* Physiological reports, 2017. **5**(18): p. e13453.